Available online at www.sciencedirect.com
ScienceDirect
Trans. Nonferrous Met. Soc. China 33(2023) 1124−1143
Transactions of Nonferrous Metals Society of China
www.tnmsc.cn

Influence of laser power on microstructure and tensile property of a new nickel-based superalloy designed for additive manufacturing

Bin WU[1,2], Jing-jing LIANG[1,3], Yi-zhou ZHOU[1], Yan-hong YANG[1,3], Jin-guo LI[1,3], Xiao-feng SUN[1]

1. Shi-changxu Innovation Center for Advanced Materials, Institute of Metal Research, Chinese Academy of Sciences, Shenyang 110016, China;
2. School of Materials Science and Engineering, University of Science and Technology of China, Shenyang 110016, China;
3. Key Laboratory of Space Manufacturing Technology, Chinese Academy of Sciences, Beijing 100094, China

Received 13 December 2021; accepted 18 July 2022

Abstract: The microstructure and tensile properties of a new Ni-based superalloy specially designed for additive manufacture (AM) were investigated under different laser power (LP) conditions. The results measured by X-ray diffraction analysis and scanning electron microscopy show that no cracks are observed in as-deposited alloy, which has typical crystallography orientation and non-equilibrium solidification dendrite/cellular morphology. The elements such as Nb, Si and Ti are enriched in the interdendritic regions, while Al, Cr and Co segregate in the dendritic cores. When the LP is low, the cellular crystals of the alloy are arranged orderly, the primary dendrite arm space (PDAS) is small, the porosity is large, the strength is high and the elongation is low. With the increase of LP, the PDAS increases, the porosity decreases, the strength decreases and the elongation increases. When the LP is elevated further, Marangoni convection effect is enhanced and shows unique impacts, that is, the disordered arrangement of cellular crystals occurs. Then, the PDAS decreases, the porosity increases, the strength increases and the elongation decreases. The smaller PDAS favors the reduction for elements segregation, as well as microstructure refinement and strength improvement. The fitting formula between PDAS and yield strength (YS) was proposed, and the concentric ring patterns inside microstructure were rationalized.

Key words: Marangoni convection; molten pool; laser power (LP); primary dendrite arm space (PDAS); segregation

1 Introduction

Superalloys have been widely used for the hot-section components of aero engines and ground gas turbines. Many traditional techniques, such as casting, forging, welding, powder metallurgy and mechanical machining, have been used to produce superalloy parts. In contrast to conventional processing methods, additive manufacturing (AM) is based on an incremental layer-by-layer manufacturing [1], which has many unique advantages, such as fabrication of complex geometry with high precision, maximum material savings, flexibility in design, and personal customization [2], as well as production without expensive tooling or forms such as punches, dies or casting molds, and thus reduces many conventional processing steps [3]. Therefore, producing superalloy components by AM becomes material research frontier nowadays.

Laser based additive manufacture [4], is the most prevailing AM technology for superalloy components. Relieving cracks during process is one research highlight because most traditional super-alloys have a feature of high cracking susceptibility.

Corresponding author: Jing-jing LIANG, Tel: +86-18624028066, E-mail: jjliang@imr.ac.cn;
Yi-zhou ZHOU, Tel: +86-13604036512, E-mail: yzzhou@imr.ac.cn
DOI: 10.1016/S1003-6326(23)66170-9

The relationship among the cracking susceptibility, the chemical composition, the microstructure and the deposition processing were explored [5−7]. Approaches, such as adjusting strengthening elements [8] or minor alloying elements [9], were used to reduce cracking. Oxides were also introduced into superalloys to achieve superior high-temperature performance [10]. Up to now, it is still a challenge to produce crack-free superalloy components. Designing superalloy materials specific for AM [2−4] becomes a common view.

Furthermore, improving properties of available AM materials is another focus. Procedure parameters, such as laser type, laser power (LP), scan speed, scan strategy, rate of feed power, as well as materials chemical compositions [11−14] are considered. Among them, laser is one of the key factors and especially highlighted. Different types of laser beams (including Gaussian beam and square-shaped flat-top beam) were adopted for comparison [15], which were found to influence dendrite growth and grains significantly; The Laves phase fraction in IN718 deposited by Gaussian distribution laser is substantially higher than that deposited by flat top laser beam [16]. Beam ellipticity also has a strong effect on the solidification microstructure [14]. Many studies also centered on the effect of laser power on both crack susceptibility and microstructure of AM materials [4,17−19]. It was found that larger LP densities can minimize the amount of cracks [12]. Semi-quantitative processing–primary dendritic arm spacing (PDAS) maps was obtained by LIANG et al [20,21], but the results can only be used in a limited scope because the effect of melt convective is neglected. XIA et al [22] considered the effect of Marangoni convection on molten pool under elevated LP in the simulation, and the results were consistent with the experiments. But the varying trend of PDAS with LP is not discussed. Generally, LP plays a crucial role in the microstructure and properties of the prepared part, as well as susceptibility of crack.

In this work, laser metal deposition (LMD) was utilized to investigate the relationship among microstructure, properties and LP. A newly-designed nickel-based superalloy specially for AM was used in the research, which is expected to keep good properties in wide processing windows. In the investigation, the relationship between PDAS and LP was discussed. Some interesting phenomena were also clarified, such as element segregation behavior, concentric circles and explanations for precipitation particle distribution, which were scarcely mentioned in current literatures. The understanding of fundamental mechanisms for those effects is indispensable for better applications of the additive manufactured (AMed) new materials.

2 Experimental

2.1 Materials

The raw material used for deposition was argon-atomized alloy powder with composition (wt.%): 4.50 (Al + Ti), 20.00 (Co + Cr), 9.20 (Hf + Mo + Nb), 0.46 (Si + C) and balance Ni. The average diameter is about 70 μm. A Co-based directional solidification superalloy, DZ40M, was used as the substrate for deposition.

2.2 Experimental procedures

The experiment was carried out on a LMD system with a CO_2 laser beam with circular profile Gaussian distribution (CP4000 made by UNITY PRIMA, TEM01*mode) included, as displayed in Fig. 1(a). The processing parameters such as beam scan velocity (23.75 mm/s), powder feed rate (10 g/min), flow rate of the powder feeding gas (10 L/min) and beam diameter (0.9 mm) were selected. Cross direction raster scanning (CDRS) was used as the laser scan path. The as-deposited part is shown in Fig. 1(b), where P1−P6 represent six different segments (16 mm × 16 mm × 60 mm)

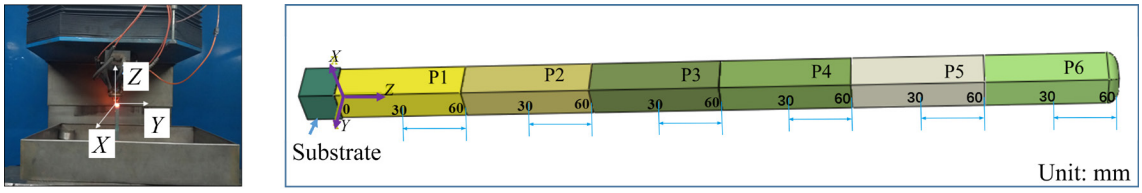

(a) (b)

Fig. 1 Photo for LMD process (a) and as-deposited part (b)

produced under six different laser power ranging from 1300 to 2000 W. Samples for observation and test were cut by wire electric discharge machine from location of 30−60 mm of each segment. The cross-sections of the samples for observation were divided into two groups as vertical (parallel to the building direction) and horizontal (perpendicular to the building direction), respectively. The samples for tensile test were cut parallel to the building direction and their sizes are displayed in Fig. 2.

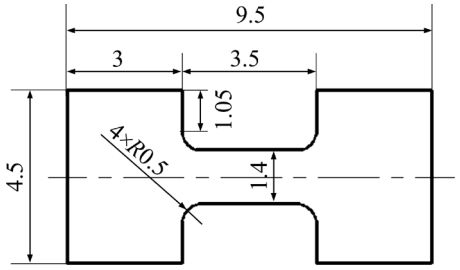

Fig. 2 Sizes of specimen for tensile test (Thickness: 1 μm, and smooth surface polished by sand paper; Unit: mm)

2.3 Microstructure characterization and mechanical testing

Samples were etched in reagent (HCl 100 mL, H_2O 100 mL, H_2SO_4 5 mL, and $CuSO_4$ 20 g) for 30−60 s after being polished by standard procedure, and then were sent for SEM (scanning electron microscopy, INSPECT F50; Netherlands, with energy dispersive X-ray spectroscopy (EDS)) observation. The value of PDAS was measured in the middle of the sample and averaged. To investigate the element segregation, EDS analyses were conducted on the cores of dendrite region (DR), interdendritic region (IR), and if necessary, on phases such as MC and Laves (MC represents metal carbides, where M represents reactive elements such as Ti, Nb and Hf; Laves is a kind of topologically close-packed phase). The beam diameter of EDS was approximately 500 nm and the acquisition time was no less than 30 s. The sampling process duplicated three times for each spot. X-ray diffraction (XRD, D8 Discover, Bruker, Germany) by Cu K_α radiation was used to identify the crystal microstructure and orientations. They were inspected in the standard θ–2θ geometry from 30° to 100° with a 0.02° step size. The resolution of angle is ±0.001°. Electron probe microanalysis (EPMA) was employed to analyze the element segregation on SHIMADZU EPMA-1610 with four spectroscopic crystals (C8H504Rb (rubidium hydrogen titanate, RbAP), C36H7004Pb (stearic acid lead salt, PBST), C5H1204 (pentaerythritol, PET) and LiF (lithium fluoride)).

Tensile tests were performed at an initial strain rate of 0.15 mm/s by a universal testing machine (Tensile tests Micro Tester INTRON 5848) at room temperature (RT) and 650 °C, respectively. The 0.2% offset yield strength (YS), the ultimate tensile strength (UTS) and elongation (E) were measured from the stress–strain curve. There are three parallel samples for each group. The fracture surfaces were studied after tensile tests by HITACHI SN 3400 SEM. Density measurements of samples (ρ_P) were taken using a temperature corrected Archimedes water displacement method. Image-Pro Plus6.0 (IPP) was used to analyze phase fraction, porosity and tensile fracture surface porosity etc. The size of the precipitation was expressed by the equivalent diameter. At least 5 typical areas are selected for each sample during statistics. JMatPro 7.0 (with Nickle based superalloy database) was used to calculate continuous cooling transformation (CCT) and time−temperature−transformation (TTT) curves, and also be employed to calculate surface tension, viscosity and phase fraction of the alloy.

3 Results and analysis

3.1 Microstructure

3.1.1 Dendrites morphology, crystallography orientation and lattice parameter

Figure 3 presents the as-deposited micro-structure prepared by LMD. It is typical cellular dendrite microstructure with only primary dendrite arms. The DR and IR occur alternatively and periodically. The DR or IR keeps orderly at lower LP, like the neat arrangement of checkerboard, but the configuration is replaced by stochastic distribution at higher LP. Furthermore, the distinct concentric circle patterns are observed at LP of 2000 W. In addition, there are no obvious laser scanning paths, and no cracks are found in all samples. Figure 4 shows PDAS for different LP. With increasing LP from 1300 to 1800 W, the value of PDAS increases from (16.60±1.32) to (47.50±4.36) μm. However, from 1800 to 2000 W, the PDAS decreases from (47.50±4.36) to (29.90±1.50) μm.

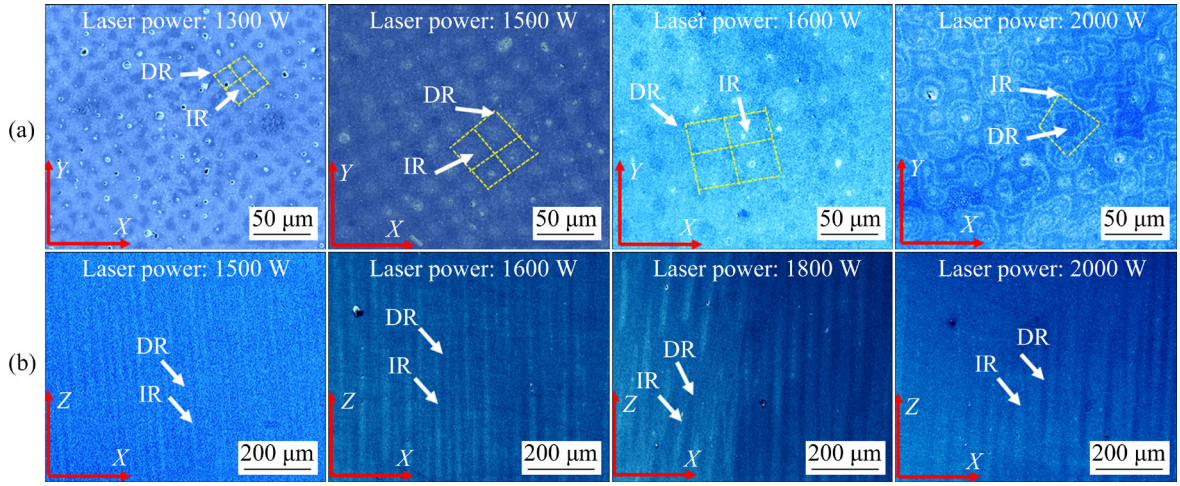

Fig. 3 SEM images of as-deposited specimens for horizontal (a) and vertical (b) cross-sections

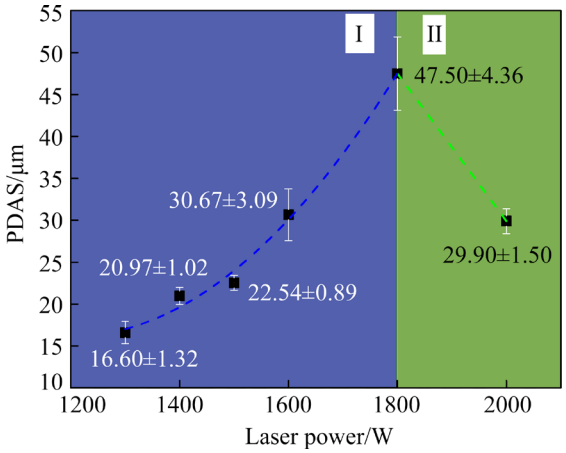

Fig. 4 Change of PDAS with LP

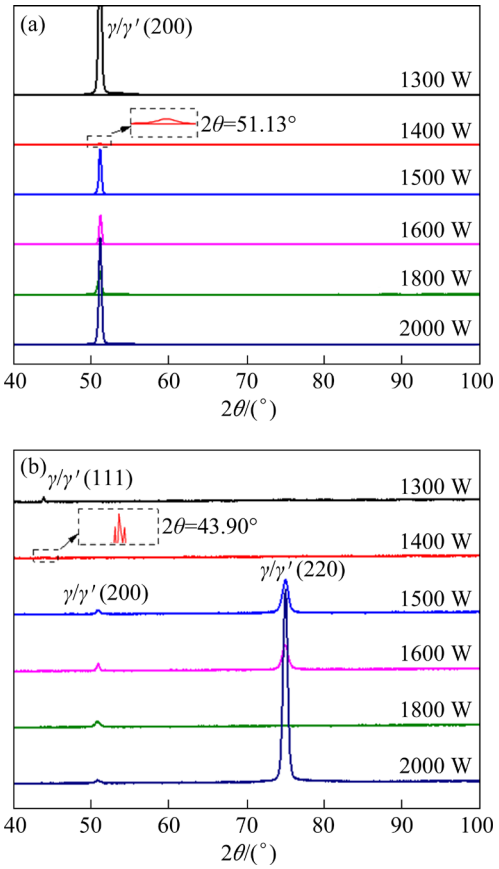

Fig. 5 XRD patterns of as-deposited samples at different LP for horizontal (a) and vertical (b) cross-sections (The peaks of sample with LP of 1400 W are very weak for experimental reasons)

XRD test results of horizontal and vertical cross-sections are displayed in Figs. 5(a) and 5(b), respectively. The horizontal cross-section displays only one diffraction peak in each samples, which corresponds to crystallography plane of {200}, and it means the samples have strong texture microstructures. The vertical cross-section displays multiple peaks, which indicates that the crystal orientation varies with different LP in X−Y plane. Obviously, the variation of LP from 1300 to 2000 W does not change the dendrite growing direction along Z axis. This phenomenon of dendrite growing direction opposite to heat flux direction is termed as constrained growth [23].

Furthermore, the peaks of the same crystallography planes for different samples are not at the same position. For example, the peak occurs at 2θ=51.15° for the sample with LP of 1300 W, while 51.17° for 2000 W. Using Bragg's law, $2d\sin\theta=n\lambda$, the lattice parameters can be calculated according to the value of 2θ obtained from XRD spectra. Table 1 lists the results, where a_v and a_h are the lattice parameters parallel and vertical to [001] direction, respectively, as demonstrated in Fig. 6. Obviously, the value of a_h increases with LP from 1300 to 1800 W and decreases with LP from 1800

Table 1 Lattice parameter for samples of different LP

Laser power/W	Calculation of a_v		Calculation of a_h	
	XRD peak	a_v/nm	XRD peak	a_h/nm
1300	γ/γ'(200)	0.356881	γ/γ'(111)	0.356591
1400	γ/γ'(200)	0.357008	γ/γ'(111)	0.357888
1500	γ/γ'(200)	0.356789	γ/γ'(220)	0.35799
1600	γ/γ'(200)	0.356573	γ/γ'(220)	0.358035
1800	γ/γ'(200)	0.357157	γ/γ'(200)	0.358838
2000	γ/γ'(200)	0.356729	γ/γ'(220)	0.357957

a_v and a_h are calculated by the corresponding XRD peaks with the strongest intensity

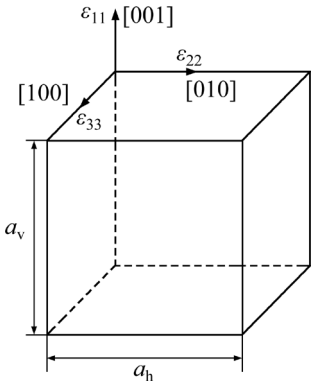

Fig. 6 Schematic for lattice parameter a_v and a_h

to 2000 W; the value of a_v has similar variation trend. It is interesting that the variation trend is similar as that of PDAS versus LP.

If a_0 is assumed as the ideal lattice parameter, the following formula can be used to evaluate the strain variation [24]:

$$\varepsilon_{11}=\frac{a_v-a_0}{a_0},\quad \varepsilon_{22}=\varepsilon_{33}=\frac{a_h-a_0}{a_0} \tag{1}$$

where ε_{11}, ε_{22} and ε_{33} are three principle strains, along crystal direction [001], [010] and [100], respectively. From Table 1, there is an inequality relation: $a_v<a_h$ for LP from 1400 to 2000 W, and thus, the inequality can be deduced: $\varepsilon_{11}<\varepsilon_{22}$ or $\varepsilon_{11}<\varepsilon_{33}$, from which the strain state or stress state of the as-deposited alloy [24] can be determined. It is noted that the case of 1300 W is an exception, where $a_v>a_h$, and then $\varepsilon_{11}>\varepsilon_{22}$ or $\varepsilon_{11}>\varepsilon_{33}$.

From previous research work [25], γ and γ' are coherent, and both contribute to the calculated lattice parameters. The lattice parameters of the pure Ni and Ni_3Al phase at RT are 0.35167 and 0.35700 nm, respectively [26]. If both phases are equal in volume fraction, the average lattice parameter should be 0.3543 nm, which does not agree with the experimental results in Table 1. It is deduced that the difference is due to solute concentration, residual stress and γ/γ' volume fraction. The as-deposited alloy is in a super-saturating state because of rapid cooling of LMD.

3.1.2 Main constituent phases

The phases of as-deposited alloy is mainly composed of γ/γ' (more than 99%), and the rest are MC carbides, Laves etc (less than 1%) [25]. The most important precipitation phase is γ', which has significant effects on mechanical properties by its morphology, particle size, distribution and volume fraction. Figure 7 shows the morphology and distribution characteristics of γ' for some samples; Table 2 presents average diameter and volume fraction of γ'. Generally, finer γ' precipitates are distributed in DR, while the coarser ones are distributed in IR for samples with LP of 1600−2000 W. Interestingly, the sample with LP of 1300 W is an exception, which shows that finer γ' precipitates are distributed in IR.

The morphology of γ' is mostly spherical, or in the middle of the transition from spherical to cubic, which is dependent on actual conditions. The IR is the part formed in the last stage of solidification, of which the solute field and temperature field are different from those of DR, usually making γ' precipitate differently. In addition, there might be more complex γ' shape, such as square, triangle and octets [26]. According to calculation results by JMatPro, the equilibrium volume fraction of γ' is about 50%, far more than 31.79%, the experimental results. This is due to the fact that precipitation of γ' is restricted by rapid cooling condition. Among all samples, the smallest γ' is found at LP of 1300 W.

MC and Laves are minor precipitates occurring in the IR of as-deposited alloy. Figure 8 presents their typical morphology with LP of 1400 W. They distribute like isolated island (horizontal cross-section) or island chains (vertical cross-section) in the shape of bulks. According to the calculation [25], MC precipitates earlier than Laves and often serves as crystal nucleus for Laves to grow. The volume fraction of them is about 0.72% from experiment data which agrees with the calculation results by JMatPro. The size of γ' adjacent to MC or Laves is usually larger. If PDAS is small, the size of Laves phase is also small. When the PDAS is larger, long stripe Laves phases

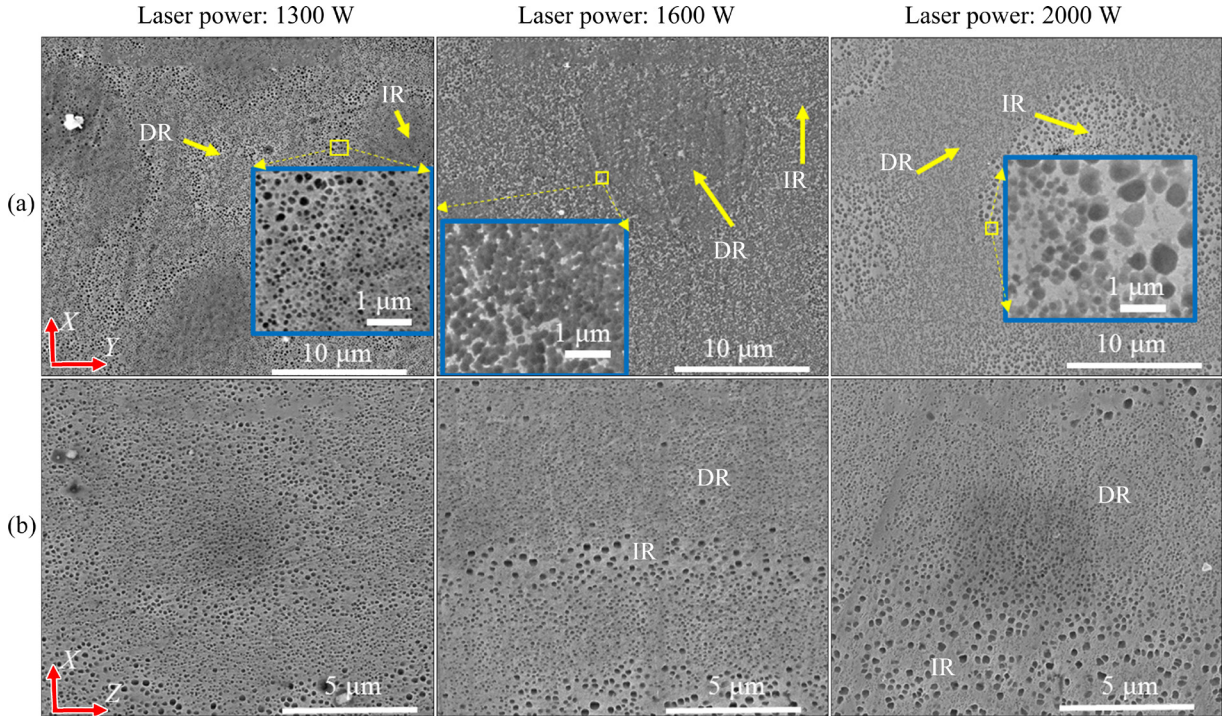

Fig. 7 SEM images showing morphology and distribution characteristics of γ' precipitates for horizontal (a) and vertical (b) cross-sections

Table 2 Average diameter and volume fraction of γ' for different LP

LP/W	Average diameter/μm	Volume fraction/%
1300	0.092	30.86
1400	0.135	37.04
1500	0.099	33.95
1600	0.115	25.31
1800	0.147	31.48
2000	0.106	32.1
Average	0.116	31.79

with larger size are occasionally found, but seldom of them are beyond 10 μm in size. Among all samples, the volume fraction of Laves for samples with LP of 2000 W is the smallest. Laves can degrade mechanical properties, especially when it has long chain shape. Therefore, many researchers tried to produce fine discrete Laves or decrease its volume fraction by AM method [16,27].

3.2 Elements segregation and loss

Figure 9 presents EDS results. By defining segregation ratio of element as $K_i=C^i_{IR}/C^i_{DR}$ (i and C represent element and its concentration, respectively), it can be found that the segregation

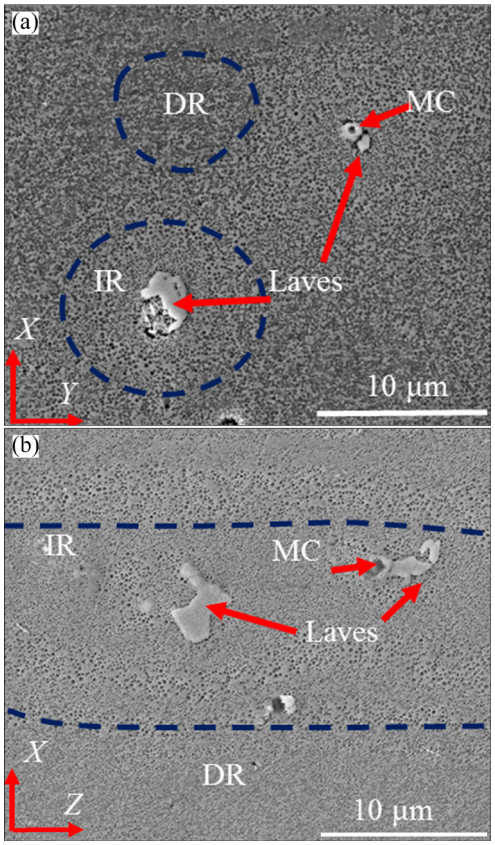

Fig. 8 Distribution characteristic of Laves and MC carbide in samples with LP of 1400 W: (a) Horizontal cross-section; (b) Vertical cross-section

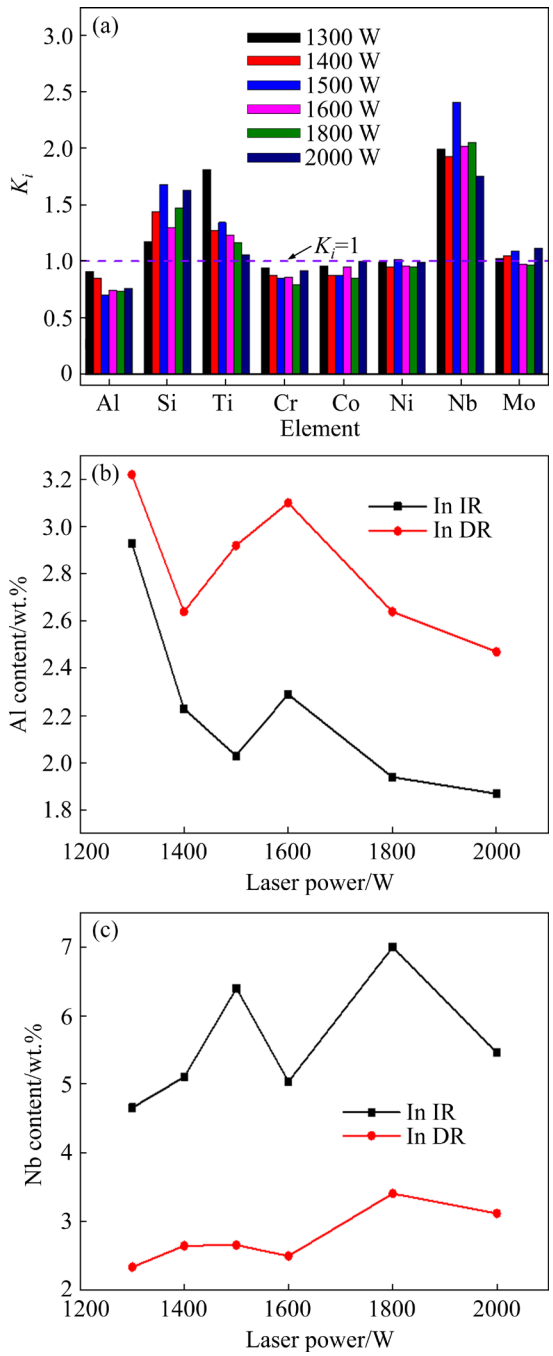

Fig. 9 EDS results: (a) Segregation ratios of elements; (b) Variation of Al content with LP; (c) Variation of Nb content with LP

trend of each element doesn't change with LP. Elements such as Nb, Si, and Ti, are enriched in the IR (K_i>1), while Al, Cr, and Co segregate in the DR (K_i<1); Mo distributes uniformly. The serious segregation elements are Si, Nb, Ti and Al.

Nb and Al are two important elements in the alloy. The results of SEM−EDS demonstrate that Al segregates in DR, while Nb in IR. Although the variation of LP has no influence on the segregation trend, the loss of element Al is closely related with LP. The higher the LP, the more loss the element Al. In addition, the loss of element Nb gets raised, as shown in Figs. 9(b, c).

Figure 10 presents EPMA results of the samples with LP of 1500 and 1300 W, and the element segregation trends with other LP values are similar. The characteristics of cellular dendrite coincide very well with those of SEM images in Fig. 3. The characteristic elements, such as C, Nb and O, are helpful to identify the possible phases such as carbides, Laves or possible oxides. For example, Laves phase or Nb-rich MC are found in IR, as denoted by arrows in Figs. 10(a, b). The Laves phase is usually expressed as $(Ni,Cr,Fe)_2$-(Nb,Mo,Ti) [3,28,29]. Nb is the important element controlling the formation of the Laves phase and it can be used as the tracer element for the evaluation of the element segregation degree [16]. Severe Nb segregation promotes the formation of brittle intermetallic and long-chained Laves phase that notably deteriorates mechanical properties, especially the hot cracking susceptibility [27,30]. Thus, LMD shows its unique advantage because the carefully selected processing parameters can produce fine and discrete Laves with smaller volume fractions, as above mentioned.

It is reported that Al has a strong tendency to segregate to IR [31−33]. However, in this study, all samples show that Al segregates in the DR. The segregation trend of Al in superalloys mainly depends on two factors: the chemical composition and the procedure parameters, and the mechanism follows the law of thermodynamics and dynamics. It is worth noting that PDAS can also be used to characterize segregation degree because the segregation cannot be beyond the scope of PDAS range. The larger PDAS favors the segregation of elements [34]. The smaller PDAS restricts Laves phase and MC carbides in IR with smaller size. Therefore, acquiring smaller PDAS by LMD is beneficial.

3.3 Results of tensile tests

3.3.1 Tensile properties

Figure 11 presents the relationship between mechanical properties and LP from tensile test. Methods of polynomial fit is utilized to quantify the variation. In Fig. 11(a), the UTS and YS curves

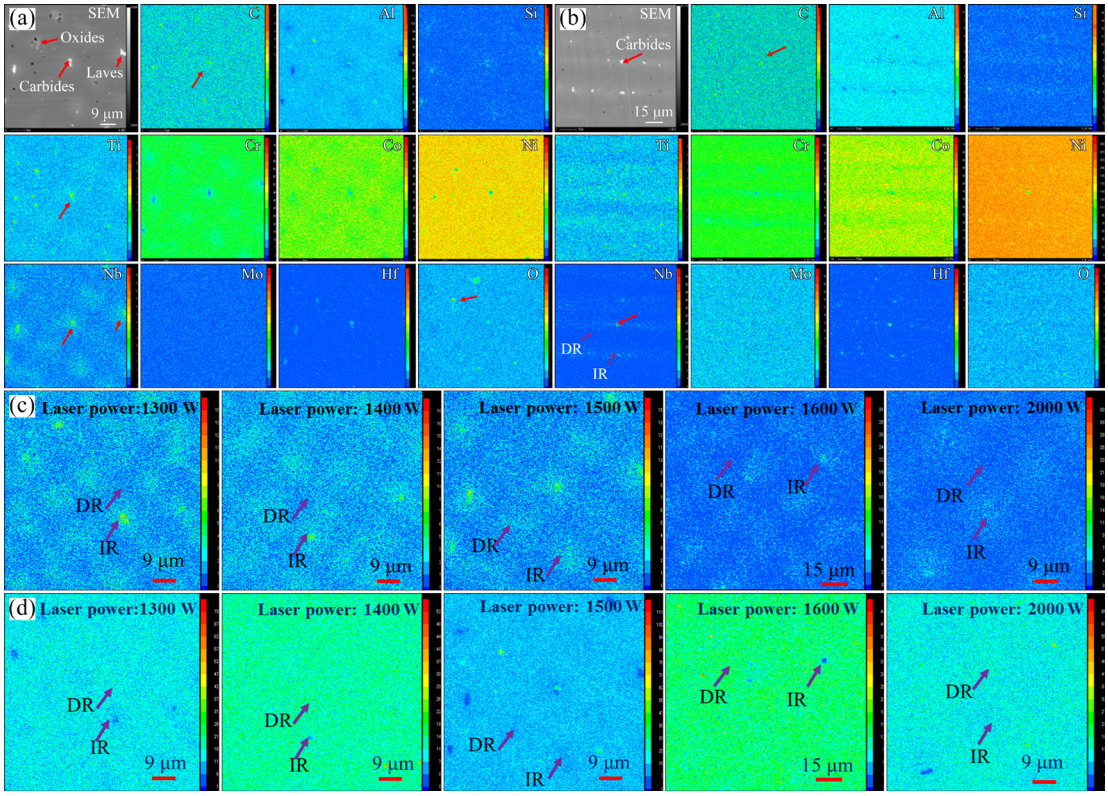

Fig. 10 Element distributions for horizontal cross-section of sample with LP of 1500 W (a) and vertical cross-section of sample with LP of 1300 W (b); element distribution for Nb (c) and Al (d) of sample with LP of 1300−2000 W (horizontal cross-section)

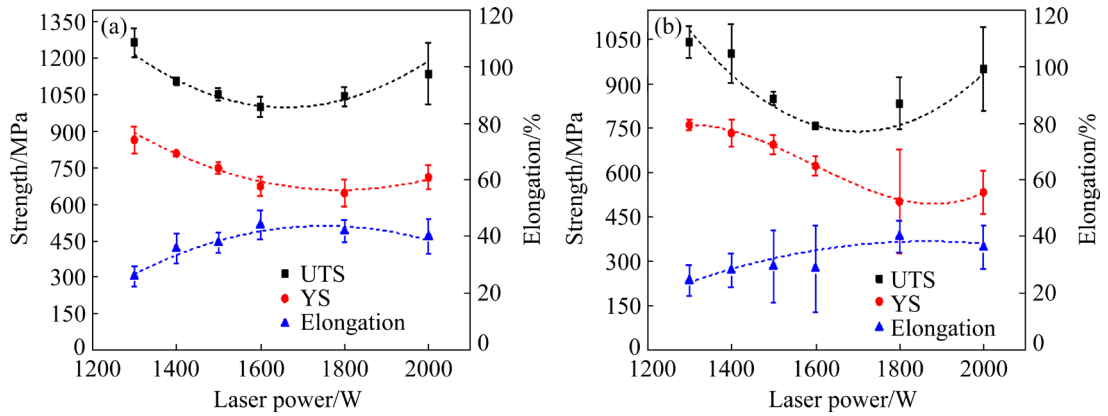

Fig. 11 Effects of LP on tensile properties: (a) At RT; (b) At 650 °C

have para-curve shape opening upward, while the elongation curve has parabola shape opening downward. In detail, when LP ranges from 1300 to 1600 W, the UTS and YS decrease monotonically from 1265 MPa (YS: 865 MPa) to 1001 MPa (YS: 675 MPa), while the elongation increases monotonically from 26% to 44%; while LP ranges from 1800 to 2000 W, the UTS and YS increase monotonically from 1042 MPa (YS: 647 MPa) to 1137 MPa (YS: 711 MPa), while the elongation decreases monotonically from 42% to 40%. Figure 11(b) presents the results performed at 650 °C, which demonstrates that UTS, YS and elongation are all reduced in value to some extent in comparison to those at RT. The err bars of RT is shorter. But the general variation of them are similar.

To quantitatively predict mechanical property for various PDAS, relationship between PDAS and YS is fitted, as shown in Fig. 12. The obtained fit equations are $y=2594x^{-1/2}+229$ with standard deviation $R^2=0.9995$ (at RT) and $y=2369x^{-1/2}+185$

with R^2=0.9993 (at 650 °C), where x and y represent PDAS and YS, respectively. Essentially, YS is dominated by its microstructure (characterized by PDAS) rather than LP. In addition, the obtained formulas are a little like Hall−Petch formula in polycrystalline alloys [35]. However, the strengthening effect of Hall–Petch relation ($\sigma=\sigma_0+kd^{-1/2}$, where σ is the YS, σ_0 is the friction stress, k is the Hall–Petch coefficient, and d is the average grain size) comes from the grain boundary, while the better YS of as-deposited alloy comes from smaller PDAS.

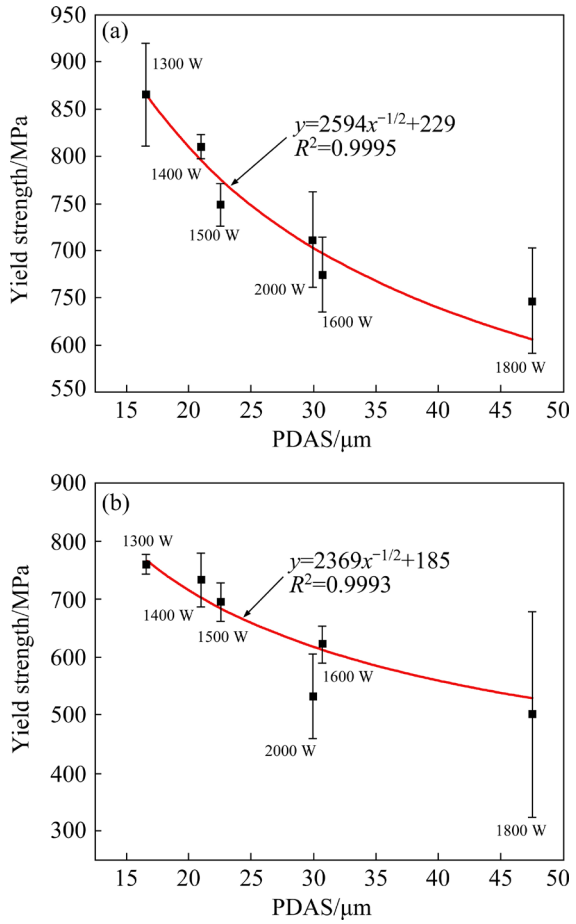

Fig. 12 Relationship between PDAS and YS at different tensile temperatures: (a) RT; (b) 650 °C

The tensile results at either RT or 650 °C show that YS decreases with the increase of PDAS, which can be attributed to the following reasons: Firstly, the smaller the PDAS is, the more uniform the properties of the alloy are. Secondly, the smaller PDAS is beneficial to forming fine and discrete Laves phase rather than long strain continuous Laves. The smaller PDAS also has effect to suppress the forming of Laves. Laves phase deteriorates mechanical properties not only by its intrinsic brittle feature, but also consuming refractory elements which is deliberately added to the alloy for improving properties. Thirdly, the eutectics and pores are refined and scattered with smaller PDAS.

3.3.2 Tensile fracture surfaces

Figure 13 presents fracture surfaces of the tensile specimen, and the inset images show the magnified morphology. A large number of parallel slip bands can be observed near the periphery of the fracture. There are lots of dimples and pores on the fracture surfaces (as denoted by arrows). Mostly, the pores are stretched out in the same direction, with parallel slip ribbons inside them. The fracture can be regarded as a ductile mode by the typical dimple feature on the fracture surfaces.

For tests at RT, the deformation and fracture of the alloy are closely related to the ⟨110⟩{111} slip system. Firstly, the tensile deformation follows Schmid law [24]: sliding initiates when the critical resolved shear stress (CRSS) is satisfied, along the direction with maximum Schmid factor offering the maximum shear stress. Secondly, parts of samples might rotate during tensile process. As shown in Fig. 13(a) for samples with LP of 1400, 1500 and 2000 W, where the intersection angle α between the original edge and the fractured one, is used to describe rotation degree. During slipping, the dislocations in the crystal usually glide in the {111} plane for both γ and γ', which often induce cracks originating on {111} plane and propagating along it. Therefore, the macroscopic fracture surface is relatively flat. In order to keep the Schmid factor at a maximum value, the fracture surface tends to decline by 45° to the direction of tensile axis (approximately parallel to ⟨001⟩ direction of the as-deposited alloy). The larger the value, the easier the slide. In addition, it is found that the fracture edges are straight for samples with LP of 1300−1500 W, while the fracture edges with LP of 1600−2000 W show obvious irregular shapes, which indicates that the former might have more uniform deformation behavior.

For tests at 650 °C, the deformation behavior is affected not only by Schmid law, but also by thermal activation. Combined with thermal and external force, cracks can originate from micro-porous aggregation location, and its propagation is not only on the {111} plane. Secondary cracks can be obviously observed on the fracture surface which

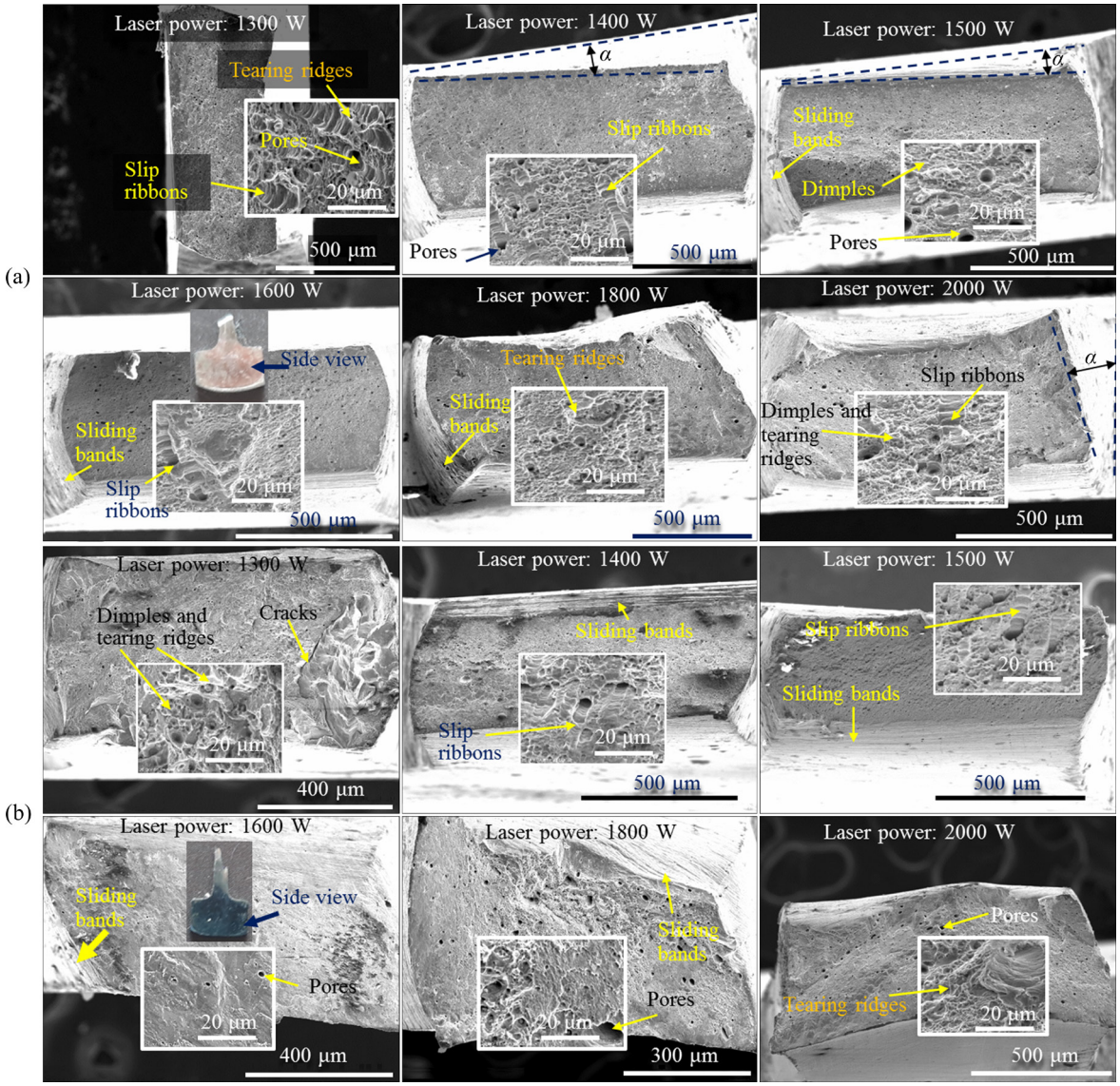

Fig. 13 SEM images showing tensile fracture surface of as-deposited alloy: (a) At RT; (b) At 650 °C

is more irregular. From the microscopic view, the mobile dislocations are often blocked in γ/γ' interface rather than cut in γ' phase due to elevated temperature, and the interfaces may become crack sources. In addition, sample rotation is not as obvious as that at room temperature, and the plasticity is also relatively lower (refer to Fig. 11). Similarly, for samples with LP of 1300−1500 W, the fracture edges are straight after tensile test, while the fracture edges of samples with LP of 1600−2000 W show obvious irregular shapes, which are more complex than those in RT tensile test.

3.4 Porosity and density

Figures 14(a, b) show density and porosity of as-deposited specimens of different LP. The relationship between the density and the LP approximately conforms to the parabola function with opening downward. The porosity versus the LP conforms to the parabola relationship with opening upward, and the fracture surface porosity for tensile tests at RT also displays the similar trend, as shown in Fig. 14(c). The porosity of the latter is significantly higher because more micro pores are aroused during tensile deformation. In addition, pores in the deposited sample are less than 10 μm in diameter.

In common sense, pores are detrimental to mechanical properties. The higher the porosity is, the lower the mechanical properties are. However, according to the experimental results, although the samples with LP of 1300 and 2000 W have higher

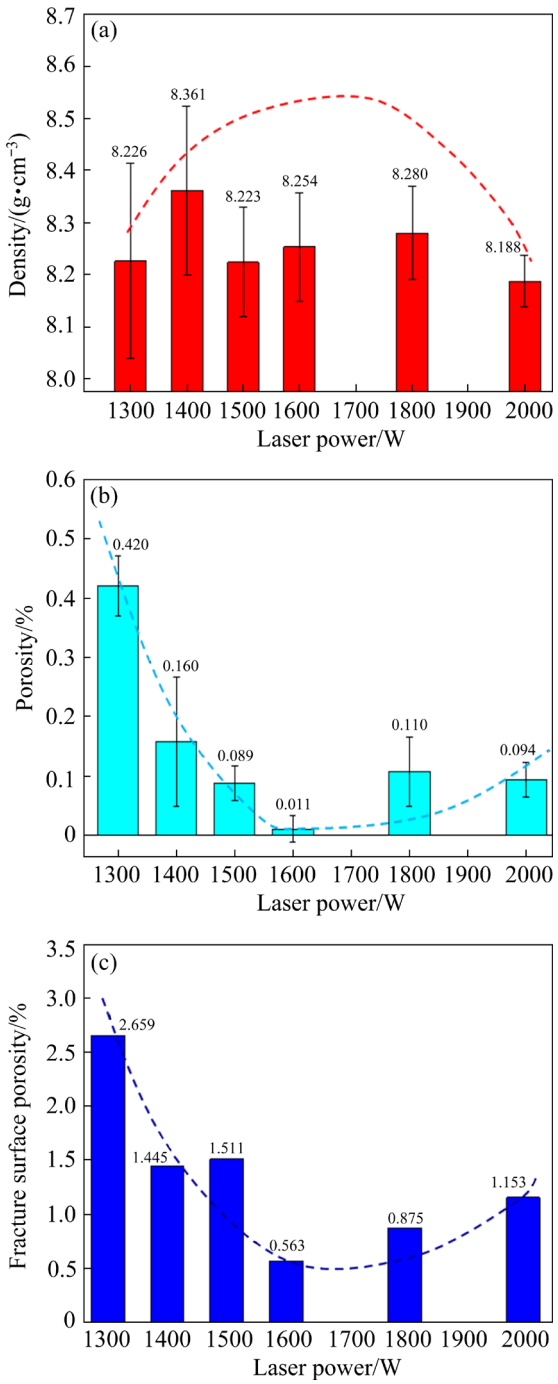

Fig. 14 Density and porosity for specimens of different LP: (a) Density; (b) Porosity; (c) Fracture surface porosity

porosity, their UTS and YS are superior to those of other samples. It is found that the sample with LP of 1600 W has the lowest microporosity, but its strength is not better than that of the others. The abnormal phenomena could be ascribed to the weakening effect of porosity offset by other strengthening effects; for example, the excellent YS for the sample with LP of 1300 W is due to its smallest PDAS as above-mentioned. Moreover, the phenomena could be ascribed to the vacancy strengthening [36] according to the concept of point defect strengthening mechanism, which means the higher porosity samples might have more vacancy strengthening effect.

4 Discussion

4.1 Solidification process

In principle, laser additive manufacturing parts are formed by the accumulation of molten pool solidification, as sketched in Fig. 15. The research of molten pool is fundamental for LMD. The type of dendrite, the PDAS, the porosity and crystal orientation of the alloy are closely related to the size and shape of the molten pool, which are the comprehensive resultant of heat, mass and momentum transfer inside the pool. Therefore, modeling and analysis of the molten pool is one of the hot spots nowadays [22,37−43].

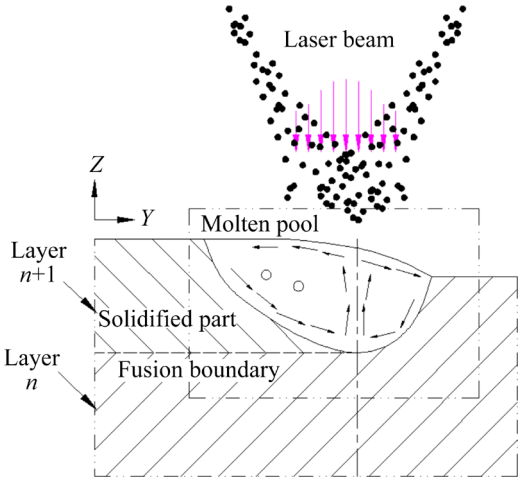

Fig. 15 Schematic of LMD process

4.1.1 Typical solidification microstructure of molten pool

Solidification map is often used to judge the morphology and size of solidification microstructures [3,39,44,45], as illustrated in Fig. 16(a), where G is thermal gradient normal to the liquid/solid interface, R is solidification rate or growth rate, and their combined forms of $G\times R$ and G/R determine the size and morphology, respectively. During LMD, the different regions of the molten pool have different G and R, thus resulting in different solidified microstructures, as illustrated in Fig. 16(b), where the microstructure of

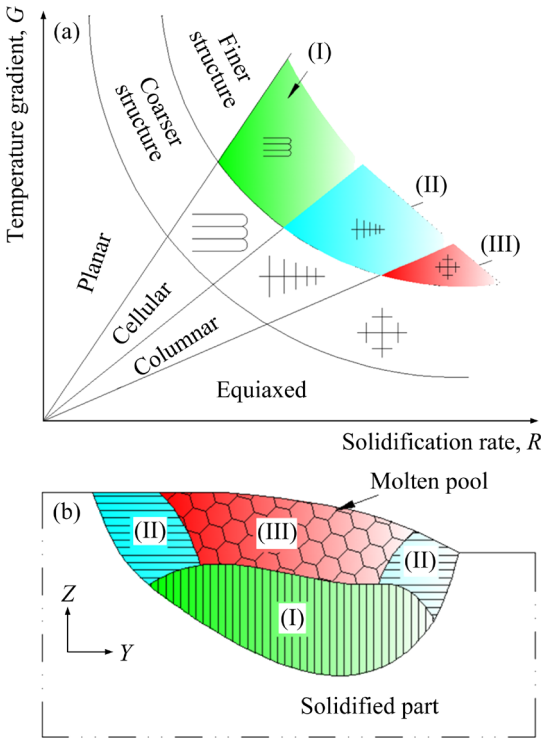

Fig. 16 Solidification map (a) and microstructure of molten pool (b)

molten pool can be roughly classified as three categories: the columnar crystal (I), growing along the deposition direction from the pool bottom, the columnar crystal (II), growing from the side wall, and the equiaxed crystal (III), growing in the upper center area. By selecting eligible processing parameters during LMD, the columnar crystal area (I) can be retained, and finally become main part of the sample, as displayed in Fig. 3, while Parts II and III are eliminated by re-melt with subsequent cyclical laser beam scanning. Of course, the final surface of the as-deposited part still keeps equiaxed crystal microstructure in the end of the process. Obviously, Part I in Fig. 16(b) is the product of constrained growth [23], where the heat flow is opposite to the dendrite growth direction during solidification, and its typical morphology is termed as "cellular" in Fig. 16(a). The experimental results demonstrate that when LP varies from 1300 to 2000 W, the value of $G\times R$ and G/R are still not beyond the cellular sector in Fig. 16(a), though their PDAS is different.

4.1.2 Influence of laser power on molten pool

4.1.2.1 Marangoni convection

The molten pool theory is fundamental for LMD processing. The shape of the molten pool, as well as the temperature field, solute field and velocity field inside it, are often affected by Marangoni convection, which have a strong correlation with thermal gradient G and solidification rate R and eventually decide the solidification microstructure.

In LMD process, energy density distributions of the heat source often follow axisymmetric Gaussian profiles [3]. When Gaussian distribution laser beam (GDLB) is utilized, the temperature at the edge of molten pool is generally lower than that of the center, and the spatial variation of temperature results in Marangoni effect, which can be depicted by following expressions [46]:

$$\tau_x = \mu\frac{\mathrm{d}u}{\mathrm{d}z} = \frac{\mathrm{d}\gamma}{\mathrm{d}T}G_x \tag{2}$$

$$\tau_y = \mu\frac{\mathrm{d}v}{\mathrm{d}z} = \frac{\mathrm{d}\gamma}{\mathrm{d}T}G_y \tag{3}$$

$$\tau_z = \mu\frac{\mathrm{d}w}{\mathrm{d}r} = \frac{\mathrm{d}\gamma}{\mathrm{d}T}G_z \tag{4}$$

where x, y and z are coordinates (m); u, v and w are velocities (m/s) along x, y and z, respectively; r is the radial distance from center of the heat source, μ is dynamic viscosity (Pa·s); T is temperature (K); γ is surface tension (N/m) and $\mathrm{d}\gamma/\mathrm{d}T$ is the surface tension gradient, also termed as the Marangoni coefficient. τ_x, τ_y and τ_z are three components of Marangoni stress along x , y and z, respectively; G_x, G_y and G_z are the temperature gradients along x, y and z, respectively. According to the value of $\mathrm{d}\gamma/\mathrm{d}T$, Marangoni effect in the molten pool can be divided into three types: (1) $\mathrm{d}\gamma/\mathrm{d}T=0$, and there is no Marangoni convection in the molten pool; $\mathrm{d}\gamma/\mathrm{d}T<0$, and Marangoni convection in the molten pool is in a form of outward convection [37]; (3) $\mathrm{d}\gamma/\mathrm{d}T>0$, and the molten pool may display a form of inward convection.

Figure 17 shows the effect of temperature on viscosity and surface tension (calculated by JMatPro) of the investigated alloy. The value of $\mathrm{d}\gamma/\mathrm{d}T$ is about -3.87×10^{-4} N/(m·K), which means when LP is high enough to drive the molten, Marangoni convection will display a form of outward convection, as sketched in Fig. 15.

4.1.2.2 Influence of Marangoni convection on porosity

The effect of Marangoni convective molten pool has been investigated by XIA et al [22]. As

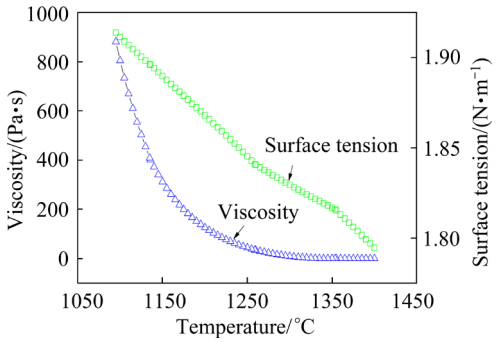

Fig. 17 Relations of viscosity and surface tension versus temperature

sharing the common mechanisms, the results are used in this research. By assuming $P1<P2<P3$ (P represents laser power), three categories are classified according to LP from weak to strong, as shown in Fig. 18(b).

(1) $P1$

In this case, Marangoni convection is small relatively and the flow rate is low because the melt viscosity is high and Marangoni stress is not high. Bubbles are not easy to escape from the melting pool. Conduction, supplemented by the natural convection, is the dominant heat transfer style.

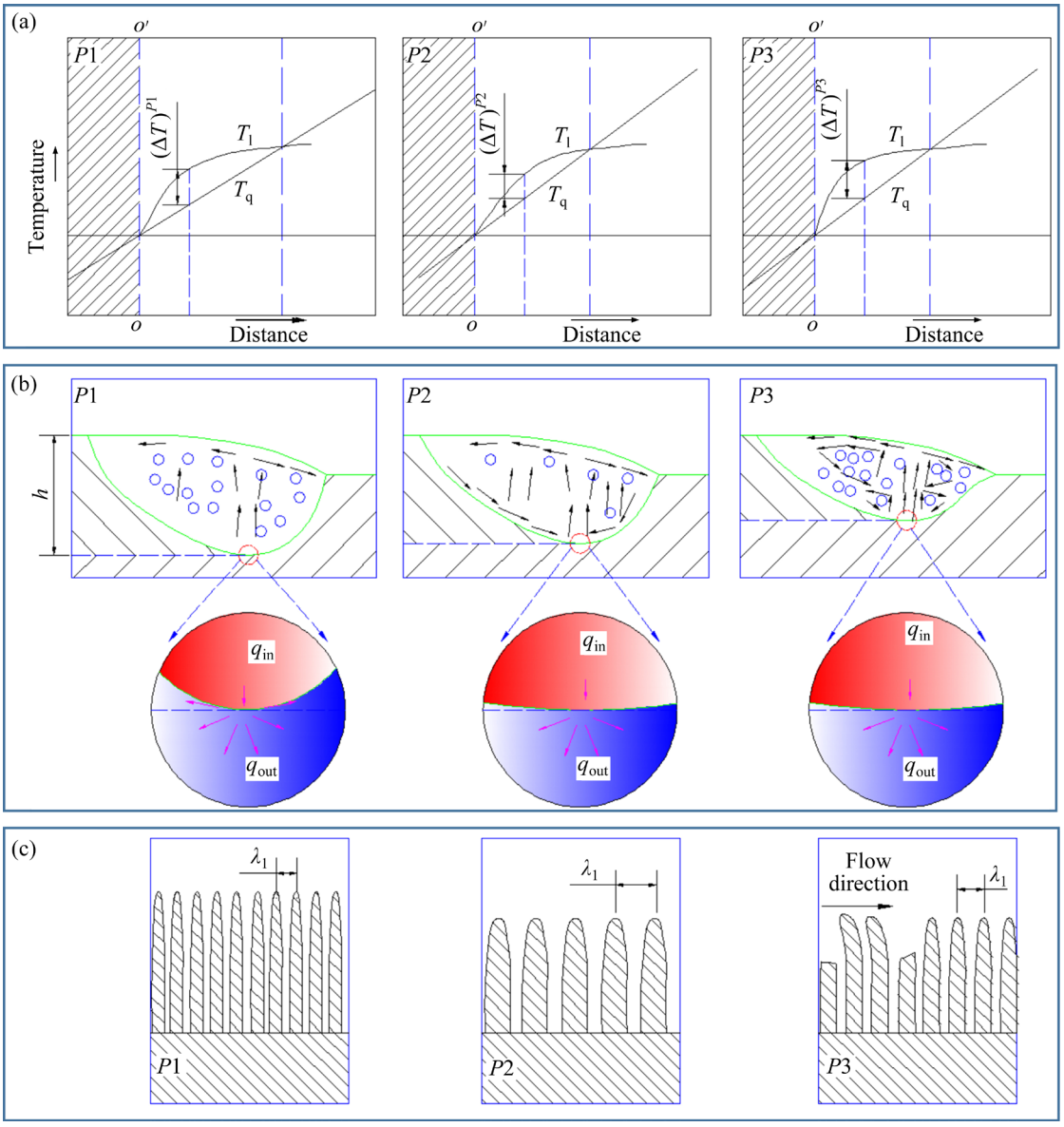

Fig. 18 Melting pool evolutions with different LP: (a) Temperature distribution in front of liquid/solid interface OO', $(\Delta T)^{P1}>(\Delta T)^{P2}$ and $(\Delta T)^{P3}>(\Delta T)^{P2}$; (b) Heat transfer at bottom of melt pool with pool height: $h^{P1}>h^{P2}>h^{P3}$; (c) Morphology of solidified microstructure, $(\lambda_1)^{P1}<(\lambda_1)^{P2}$ and $(\lambda_1)^{P3}<(\lambda_1)^{P2}$ (λ_1, ΔT and h are the PDAS, supercooling and pool height, respectively; T_l and T_q are the liquidus temperature corresponding to the alloy composition and measurable temperature [23] imposed by the heat flux, respectively; P represents LP and $P1< P2<P3$)

(2) *P*2

The elevated LP heats the pool to a higher temperature, the viscosity of the melt decreases, Marangoni stress increases, and the melt flow rate increases. The molten pool becomes wider and shallower. Bubbles can easily float and escape from the pool.

(3) *P*3

In this case, the liquid velocity can raise up by one order of magnitude [47], and Marangoni convection is enhanced and makes the flow rate large enough to form a vortex in the melt, trapping the bubble in the melt. The predominant heat transfer is convective rather than conduction.

*P*1, *P*2 and *P*3 approximately correspond to 1300−1500, 1600−1800 and 2000 W in this work, respectively. The pore statistics of SEM images show that the porosity is 0.011% at 1600 W, 0.420% at 1300 W and 0.094% at 2000 W, as shown in Fig. 14(b), which agrees well with the above classification.

4.1.2.3 Influence of Marangoni convection on PDAS

PDAS is the very important microstructure feature and many research work [7,20,34,48,49] have centered on it. LIANG et al [20] found that with the increase of LP, PDAS first decreases and then increases by ignoring the effects of solidification latent heat and convection in their model. But some of their results do not agree with our experiment results. When the diameter of laser beam spot is larger than that of molten pool and the convection effect is very small, their approach can be accurate. However, when the laser beam spot is smaller than the melt pool, especially at high LP (such as 2000 W), Marangoni convection can not be neglected because it influences solidification strongly, which can lead to the variation of PDAS significantly.

Intrinsically, PDAS is determined by the solidification conditions. Quantitative formulas are proposed to relate PDAS to solidification conditions [20,23,34,48], and one of the simplest is

$$\lambda_1=NG^{-a}V^{-b}\ (0<a,\ b<1) \tag{5}$$

where λ_1 is the PDAS; a, b, and N are material-dependent parameters; G is the temperature gradient and V is the dendritic growth velocity, respectively. Generally, a=0.5 and b=0.25. N can be determined by experiments. Solidification conditions, such as G and V, are very difficult to measure during LMD. However, according to Marangoni convective effect on molten pool [22], some semi-quantitative analysis can be concluded, as illustrated in Fig. 18(b).

Firstly, during the LMD, the molten pool undergoes following stages: forming and growing through alloy melt, standstill, and shrinking with solidification. When the molten pool reaches its maximum volume, the pool comes to its standstill stage, no liquid/solid interface migrates, and the input and output of heat flux q (denote as q_{in} and q_{out}, respectively) through the interface are equal ($q_{in}=q_{out}$). Before the instant, $q_{in}>q_{out}$, and after that, it must be $q_{in}<q_{out}$. Obviously, q is the controlling factor. When the condition of $q_{in}<q_{out}$ is satisfied, the melt pool begins its directional solidification from the bottom part (Figs. 18(b, c)).

If a micro unit cell is extracted at the bottom of the molten pool, as shown in Fig. 18(b), it is easy to see that $(q_{out})^{P1}>(q_{out})^{P2}$ because the case of *P*1 has more heat transfer passages; On the other hand, under condition of *P*1<*P*2, $(q_{in})^{P1}<(q_{in})^{P2}$. According to energy conservation principle, solidification velocity R can be expressed as

$$R=(q_{out}-q_{in})/(\rho L) \tag{6}$$

where L is the latent heat, and ρ is the density of solid phase.

Meanwhile, the dendrite growth rate and solidification rate have the relationship [50,51]:

$$V=R/\cos\psi \tag{7}$$

where ψ is the angle between normal of the solid/liquid interface and the dendrite growth direction. By combining with Eqs. (5)−(7), $V^{P1}>V^{P2}$ and $(\lambda_1)^{P1}<(\lambda_1)^{P2}$ are obtained (In this case, PDAS is mainly dependent on dominant factor V).

Secondly, according to solidification theory, crystal growth needs a certain degree of super-cooling as driving force, and the supercooling can be expressed as [3]

$$\Delta T=\Delta T_C+\Delta T_T+\Delta T_K+\Delta T_R \tag{8}$$

where ΔT_C, ΔT_T, ΔT_K, and ΔT_R are the undercooling contributions associated with the solute diffusion, thermal diffusion, attachment kinetics and solid/liquid interface curvature, respectively. For most metallic alloys, under ordinary solidification conditions, ΔT_T, ΔT_K and ΔT_R are small and solute undercooling ΔT_C predominates. ΔT_C is also termed

as constitutional supercooling [23].

During solidification of case *P*3, the solute is continually rejected from solid to the liquid and quickly taken away due to convection, which remarkably increases dendrite growth rate, i.e., $V^{P2}<V^{P3}$. Although the temperature gradient G varies concurrently, its effects on the PDAS is relatively minor. Furthermore, much laser energy transfers to convective kinetic energy rather than heat energy. Therefore, $(\lambda_1)^{P2}>(\lambda_1)^{P3}$ is obtained.

In summary, the relationship between PDAS and LP in Fig. 4 can be rationalized from $(\lambda_1)^{P1}<(\lambda_1)^{P2}$ and $(\lambda_1)^{P2}>(\lambda_1)^{P3}$. Furthermore, in the case of low LP, DR and IR alternates orderly like chessboard because the fixed scanning of the laser beam offers regular temperature field and solute field. Once the PDAS is established, it will not change during the solidification process [23]. However, the mentioned physical fields are altered by enhanced Marangoni convection at higher LP, and the dendrite inclines to grow along flow direction [51]. Therefore, the arrangement of DR and IR becomes disordered when the LP is raised to 2000 W. The broken dendrite by strong convection also contributes to the stochastic distribution, as illustrated in Fig. 18(c).

Finally, at small undercooling, adjacent to melting point T_f, the actual growth rate of the solid/liquid interface can be obtained from the expression [23]:

$$V=K_{hkl}\Delta T \tag{9}$$

where K_{hkl} is the growth rate coefficients, from which, it could be deduced that $(\Delta T)^{P1}>(\Delta T)^{P2}$ and $(\Delta T)^{P2}<(\Delta T)^{P3}$; the former is mainly due to thermal diffusion while the latter is caused by solute diffusion under enhanced Marangoni convection. Figure 18(a) presents the schematic diagram.

4.2 Solid state phase transformation kinetics for γ and γ'

4.2.1 Effect of segregation on precipitation kinetics

The results of experiment show that the size of γ' in the DR is smaller than that in IR for LP of 1400−2000 W; while for LP of 1300 W, γ' in the DR has larger size than that in IR, as denoted in Fig. 7. It is inferred that local compositional variations are responsible for the phenomena. To verify the conjecture, EDS is used to measure the chemical composition of DR and IR. According to the acquired data and with the help of JMatPro, CCT and TTT diagrams are created, as shown in Fig. 19, which demonstrates the fraction of the phase transformation as a function of time and temperature [52]. More importantly, the phase transformation supercooling (ΔT) can be reflected from the plots, and the curves located on the upper left have larger supercooling than those on the bottom right under same cooling rate. Obviously, the IR with LP of 1300 W and the DR with LP of 1600 or 2000 W, have larger supercooling. The nucleation of γ' is strongly dependent on supercooling: the larger the supercooling, the larger the number density of γ' precipitates. Therefore, the IR with LP of 1300 W and the DR with LP of 1600 or 2000 W should have larger number density of γ' precipitates, which leads to the smaller size for γ' particles. The kinetics analysis agrees with observed experimental results well.

Furthermore, the experiment data show that the volume fraction of γ' in IR is larger than that in DR. This is due to the overall molar fraction of γ' forming elements, such as Al, Ti and Nb, controlling the final volume fraction of γ'. Although Al is enriched in DR, the total molar fraction of γ' forming elements in IR is more than that in DR. In addition, the experimental results show that the size and fraction of γ' adjacent to Laves are usually larger, which can be ascribed to the fact that Nb trapped in the Laves phase is released and diffuses to its surrounding during heating cycling, and thus the γ' growth is promoted. Finally, CCT or TTT curve of 1300 W is closer to nominal one, which indicates that the smaller the LP is, the less the loss of the alloy elements.

4.2.2 Effect of thermal cycling on as-deposited microstructure

Concentric circle patterns are often observed at elevated LP in the as-deposited microstructure, as displayed in Fig. 3(a). The higher the LP is, the more distinct the circles are. Figure 20(a) presents the magnified detail of sample with LP of 2000 W. Seldom literature rationalizes this interesting phenomenon. The underlying mechanism is discussed here.

During the growth of the γ dendrite, solute is continually rejected from the solid to the liquid. Hence, the concentration in the liquid continues to increase. As a result, the solute concentration C

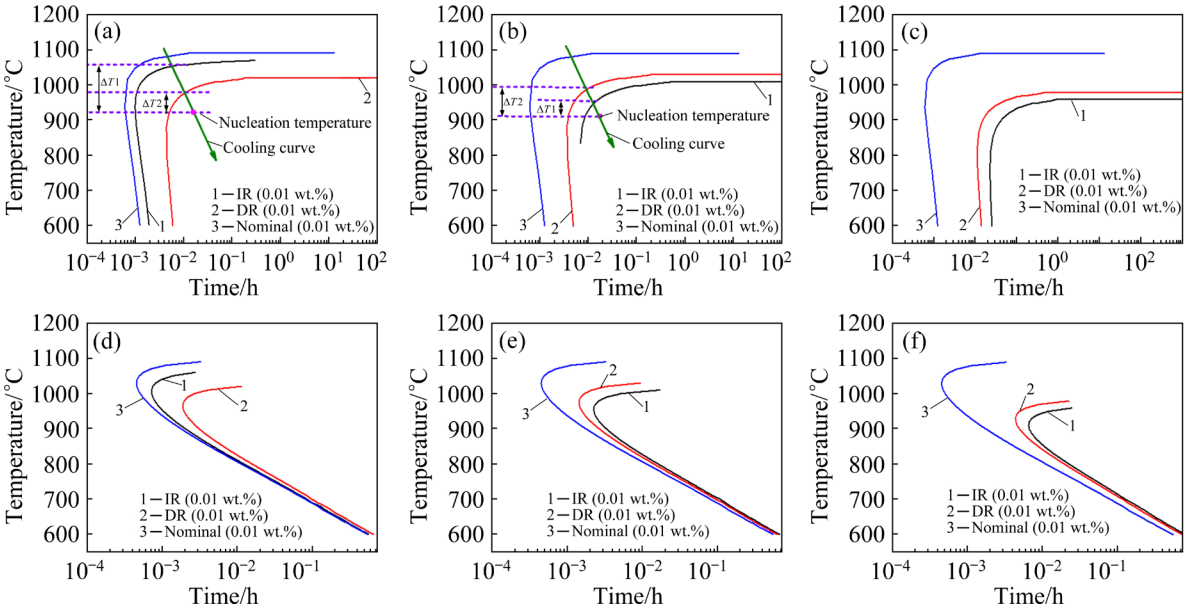

Fig. 19 Typical CCT (a−c) and TTT (e−f) curves of IR, DR and nominal composition (All lines represent 0.01 wt.% precipitation of γ'): (a, d) LP of 1300 W, (b, e) LP of 1600 W; (c, f) LP of 2000 W

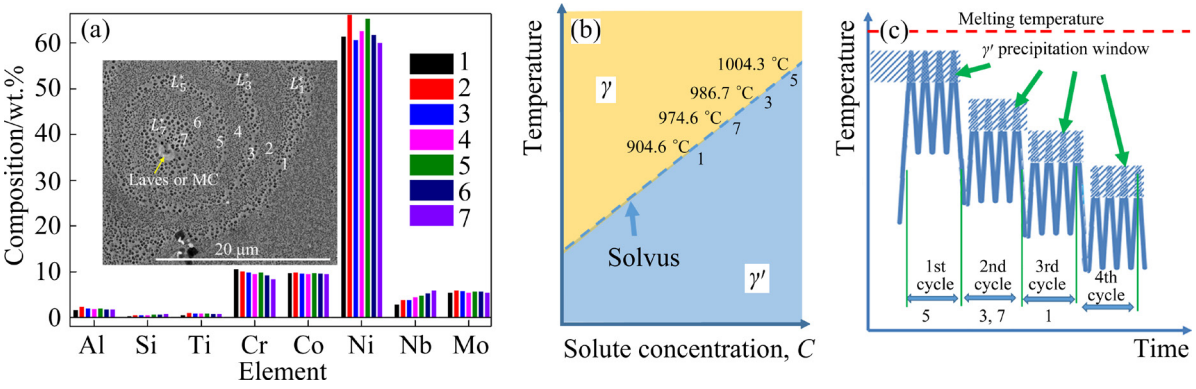

Fig. 20 Concentric circle patterns obtained at LP of 2000 W and corresponding elements composition obtained from EDS (a); Solvus for $\gamma'\rightarrow\gamma$ (b); Time−temperature history diagram during LMD (c)

gradually increases from the dendrite core to the interdendritic region with solidification, which can also be assumed as numerous iso-concentration loop collections. In subsequent cooling, different solute concentrations have corresponding phase transformation temperature T_C, the collection of which is solvus, as illustrated in Fig. 20(b). During LMD process, the as-deposited alloy endures cycling thermal history like steps or ladder [52], as schematically depicted in Fig. 20(c). According to thermodynamics, the phase transformation of $\gamma'\rightarrow\gamma$ occurs when temperature is above T_C; similarly $\gamma\rightarrow\gamma'$ occurs when temperature is below T_C.

Assuming T_i* is the phase transformation temperature for the thermal cycle i, and the corresponding critical concentration is C_i*, when the deposited alloy is heated up to T_i*, no phase transformation occurs in the region with concentration $C>C_i$*, while for those regions with $C<C_i$*, phase transformation of $\gamma'\rightarrow\gamma$ occurs according to thermodynamics. Therefore, there should be an iso-concentration loop (or line) L_i* where $C=C_i$*, and the loop L_i* becomes the dividing line, with partially dissolved γ' particle residues nearby. In the subsequent rapid cooling, the region outside loop L_i*, precipitation of $\gamma\rightarrow\gamma'$ occurs, but there is no phase transformation inside loop L_i*. Furthermore, on the loop L_i*, the nucleation process is no longer required during precipitation due to the existing of γ' particle

residues, and thus γ' particle can grow faster and acquires more solute elements, which hampers the γ' growing of other regions. Thus, larger γ' particles on loop L_i* form an obvious line. In this way, Loops 1, 3, 5 and 7 come into being, which form concentric circle collections the patterns is termed as "Wu−Liang−Zhou circle" (WLZ circle) here.

Figure 20(a) also presents the chemical composition obtained from SEM−EDS for Sites 1−7. With the aid of JMatPro, the corresponding transition temperature T_i* values of 1, 3, 5 and 7 are figured out, as displayed in Fig. 20(b). CCT and TTT curves are also plotted according to compositions of Circles 1, 3, 5 and 7, as shown in Fig. 21. Theoretically, as the solute concentration in the alloy decreases in the sequence of 7, 5, 3 and 1, the value of T_i* decreases accordingly. However, Loops 5, 3 and 1 follow the sequence, while Loop 7 is an exception. This is because the solute concentration of Site 7 is high enough to promote precipitation of Laves or MC, which consumes a lot of solute. Therefore, the real concentration for γ/γ' is not as high as measured and the corresponding T_7* is not the highest.

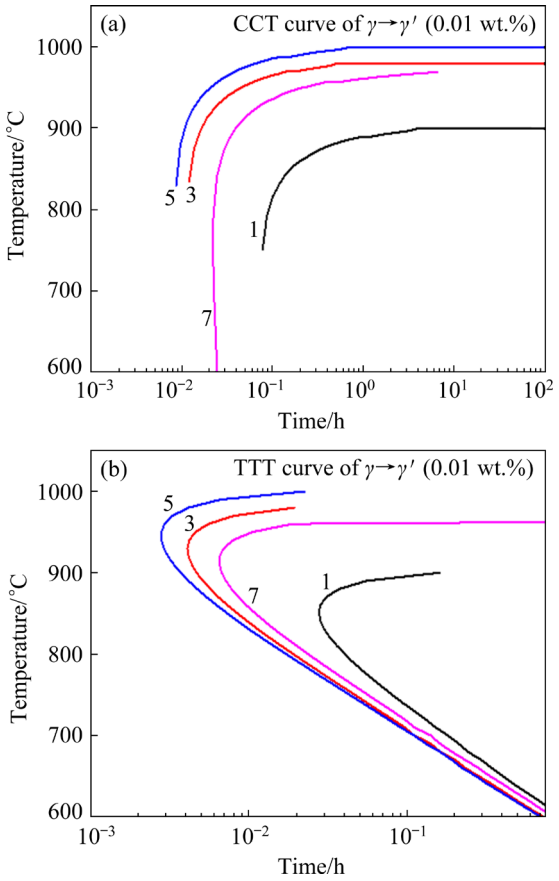

Fig. 21 CCT (a) and TTT (b) curves of different concentric circles in Fig. 20

5 Conclusions

(1) The PDAS of the alloy increases from (16.60±1.32) to (47.50±4.36) μm when laser power increases from 1300 to 1800 W, while it decreases down to (29.90±1.5) μm when the laser power is 2000 W. The results are closely related to the different heat transfer modes caused by LP.

(2) The dendrites are rich in Al, Cr and Co, while the interdendrites are rich in Nb, Ti, and Si. For LP of 1400−2000 W, the volume fraction and size of γ' in the DR are smaller compared with those in IR region. For LP of 1300 W, the size of γ' is larger in the DR. The difference comes from their composition variation.

(3) Tensile tests at room temperature and 650 °C show that UTS, YS and elongation are strongly related to PDAS. With the decreasing of PDAS, UTS and YS of the alloy increase, while the elongation decreases. Smaller PDAS is beneficial to the segregation reduction and Lavas or MC refinement.

(4) When laser power is high, the enhanced Marangoni convection can significantly affect the shape, the temperature field distribution and solute field distribution of the molten pool, thus changing the microstructure and properties of the alloy.

Acknowledgments

The authors are grateful for the financial supports from the National Science and Technology Major Project, China (No. Y2019-VII-0011-0151), and the National Natural Science Foundation of China (No. 51771190)

References

[1] LI Neng, HUANG Shuai, ZHANG Guo-dong, QIN Ren-yao, LIU Wei, XIONG Hua-ping, SHI Gong-qi, BLACKBURN J. Progress in additive manufacturing on new materials: A review [J]. Journal of Materials Science & Technology, 2019, 35: 242−269.

[2] TUAN D N, ALIREZA K, GABRIELE I, KATE T Q N, DAVID H. Additive manufacturing (3D printing): A review of materials, methods, applications and challenges [J]. Composites Part B−Engineering, 2018, 143: 172−196.

[3] DEBROY T, WEI H L, ZUBACK J S, MUKHERJEE T, ELMER J W, MILEWSKI J O, BEESE A M, WILSON-HEID A, DE A, ZHANG W. Additive manufacturing of metallic components−Process, structure and properties [J]. Prog Mater Sci, 2018, 92: 112−224.

[4] GU D D, MEINERS W, WISSENBACH K, POPRAWE R. Laser additive manufacturing of metallic components: Materials, processes and mechanisms [J]. International Materials Reviews, 2012, 57: 133−164.

[5] ZHOU Z P, HUANG L, SHANG Y J, LI Y P, JIANG L, LEI Q. Causes analysis on cracks in nickel-based single crystal superalloy fabricated by laser powder deposition additive manufacturing [J]. Materials & Design, 2018, 160: 1238−1249.

[6] QIU C L, CHEN H X, LIU Q, YUE S, WANG H M. On the solidification behaviour and cracking origin of a nickel-based superalloy during selective laser melting [J]. Materials Characterization, 2019, 148: 330−344.

[7] ACHARYA R, BANSAL R, GAMBONE J J, DAS S. A microstructure evolution model for the processing of single-crystal alloy CMSX-4 through scanning laser epitaxy for turbine engine hot-section component repair (Part II) [J]. Metallurgical and Materials Transactions B−Process Metallurgy and Materials Processing Science, 2014, 45: 2279−2290.

[8] HARRISON N J, TODD I, MUMTAZ K. Reduction of micro-cracking in nickel superalloys processed by selective laser melting: A fundamental alloy design approach [J]. Acta Materialia, 2015, 94: 59−68.

[9] TOMUS D, ROMETSCH P A, HEILMAIER M, WU X H. Effect of minor alloying elements on crack-formation characteristics of Hastelloy-X manufactured by selective laser melting [J]. Additive Manufacturing, 2017, 16: 65−72.

[10] TAN Li-ming, WANG Guo-wei, GUO Yu, FANG Qi-hong, HUANG Lan. Additively manufactured oxide dispersion strengthened nickel-based superalloy with superior high temperature properties [J]. Virtual and Physical Prototyping, 2020, 15: 555−569.

[11] WANG Y C, SHI J. Texture control of Inconel 718 superalloy in laser additive manufacturing by an external magnetic field [J]. Journal of Materials Science, 2019, 54: 9809−9823.

[12] WANG F, WU X H, CLARK D. On direct laser deposited Hastelloy X: Dimension, surface finish, microstructure and mechanical properties [J]. Materials Science and Technology, 2011, 27: 344−356.

[13] SONG H Y, LEI J B, XIE J C, WU S K, WANG L T, SHOU W. Laser melting deposition of K403 superalloy: The influence of processing parameters on the microstructure and wear performance [J]. Journal of Alloys and Compounds, 2019, 805: 551−564.

[14] ROEHLING T T, WU S S Q, KHAIRALLAH S A, ROEHLING J D, SOEZERI S S, CRUMB M F, MATTHEWS M J. Modulating laser intensity profile ellipticity for microstructural control during metal additive manufacturing [J]. Acta Materialia, 2017, 128: 197−206.

[15] WANG Ya-chao, SHI Jing. Developing very strong texture in a nickel-based superalloy by selective laser melting with an ultra-high power and flat-top laser beam [J]. Materials Characterization, 2020, 165: 1−10.

[16] CHEN Y, GUO Y B, XU M J, MA C F, ZHANG Q L, WANG L, YAO J H, LI Z G. Study on the element segregation and Laves phase formation in the laser metal deposited IN718 superalloy by flat top laser and gaussian distribution laser [J]. Materials Science and Engineering A, 2019, 754: 339−347.

[17] RAMAKRISHNAN A, DINDA G P. Direct laser metal deposition of Inconel 738 [J]. Materials Science and Engineering A, 2019, 740: 1−13.

[18] RAMAKRISHNAN A, DINDA G P. Microstructure and mechanical properties of direct laser metal deposited Haynes 282 superalloy [J]. Materials Science and Engineering A, 2019, 748: 347−356.

[19] KONG D C, DONG C F, NI X Q, ZHANG L, MAN C, YAO J Z, JI Y C, YING Y P, XIAO K, CHENG X Q, LI X G. High-throughput fabrication of nickel-based alloys with different Nb contents via a dual-feed additive manufacturing system: Effect of Nb content on microstructural and mechanical properties [J]. Journal of Alloys and Compounds, 2019, 785: 826−837.

[20] LIANG Y J, LI A, CHENG X, PANG X T, WANG H M. Prediction of primary dendritic arm spacing during laser rapid directional solidification of single-crystal nickel-base superalloys [J]. Journal of Alloys and Compounds, 2016, 688: 133−142.

[21] LIANG Y J, CHENG X, LI J, WANG H M. Microstructural control during laser additive manufacturing of single-crystal nickel-base superalloys: New processing-microstructure maps involving powder feeding [J]. Materials & Design, 2017, 130: 197−207.

[22] XIA M J, GU D D, YU G Q, DAI D H, CHEN H Y, SHI Q M. Selective laser melting 3D printing of Ni-based superalloy: Understanding thermodynamic mechanisms [J]. Science Bulletin, 2016, 61: 1013−1022.

[23] KURZ W, FISHER D J. Fundamentals of solidification [M]. Switzerland: Trans Tech Publications, 1998.

[24] MEYERS M A, CHAWLA K K. Mechanical behavior of materials [M]. 2nd ed. Cambridge: Cambridge University Press, 2009: 71−89, 374−386.

[25] WU Bin, LIANG Jing-jing, YANG Yan-hong, LI Jin-guo, ZHOU Yi-zhou. Phase constitution,microstructure and mechanical properties of a Ni-based superalloy specially designed for additive manufacturing [J]. China Foundry, 2021, 18: 397−408.

[26] REED R C. The superalloys fundamentals and applications [M]. Cambridge: Cambridge University Press, 2006.

[27] XIAO H, LI S M, XIAO W J, LI Y Q, CHA L M, MAZUMDER J, SONG L J. Effects of laser modes on Nb segregation and Laves phase formation during laser additive manufacturing of nickel-based superalloy [J]. Materials Letters, 2017, 188: 260−262.

[28] GUO Jian-ting. Materials science and engineering for superalloys. [M]. Beijing: Science Press, 2008. (in Chinese)

[29] SUN F, GU Y F, YAN J B, XU Y X, ZHONG Z H, YUYAMA M. Creep deformation and rupture mechanism of an advanced wrought Ni−Fe-based superalloy for 700 degrees C class A−USC steam turbine rotor application [J]. Journal of Alloys and Compounds, 2016, 687: 389−401.

[30] NIE P L, OJO O A, LI Z G. Numerical modeling of

microstructure evolution during laser additive manufacturing of a nickel-based superalloy [J]. Acta Materialia, 2014, 77: 85−95.

[31] HUANG M, ZHANG G, WANG D, GE Z C, LU Y Z, JIANG X W, LOU L H. Dendritic branching patterns in platforms of complex Ni-based single crystal castings [J]. China Foundry, 2019, 16: 110−117.

[32] HU Y L, LIN X, LI Y L, WANG J, ZHANG S Y, LU X F, HUANG W D. Effect of heat treatment on the microstructural evolution and mechanical properties of GH4099 additive-manufactured by directed energy deposition [J]. Journal of Alloys and Compounds, 2019, 800: 163−173.

[33] CUI R J, HUANG Z H. Microstructual evolution and stability of second generation single crystal nickel-based superalloy DD5 [J]. Transactions of Nonferrous Metals Society of China, 2016, 26: 2079−2085.

[34] SZELIGA D. Microstructure refinement of single crystal Ni-based superalloy by improvement of thermal radiation shielding in the industrial-scale Bridgman solidification process [J]. International Communications in Heat and Mass Transfer, 2020, 118: 1−10.

[35] KOZAR R W, SUZUKI A, MILLIGAN W W, SCHIRRA J J, SAVAGE M F, POLLOCK T M. Strengthening mechanisms in polycrystalline multimodal nickel-base superalloys [J]. Metallurgical and Materials Transactions A, 2009, 40: 1588−1603.

[36] AN J L, WANG L, SONG X, LIU Y, GAI Z Y, CAO X Z. Improving mechanism of both strength and ductility of GH4169 alloy induced by electric-pulse treatment [J]. Materials Science and Engineering A, 2018, 724: 439−443.

[37] ZHANG D Y, ZHANG P D, LIU Z, FENG Z, WANG C J, GUO Y W. Thermofluid field of molten pool and its effects during selective laser melting (SLM) of Inconel 718 alloy [J]. Additive Manufacturing, 2018, 21: 567−578.

[38] WOLFF S J, GAN Z T, LIN S, BENNETT J L, YAN W T, HYATT G, EHMANN K F, WAGNER G J, LIU W K, CAO J. Experimentally validated predictions of thermal history and microhardness in laser-deposited Inconel 718 on carbon steel [J]. Additive Manufacturing, 2019, 27: 540−551.

[39] SONG J, CHEW Y X, BI G J, YAO X L, ZHANG B C, BAI J M, MOON S K. Numerical and experimental study of laser aided additive manufacturing for melt-pool profile and grain orientation analysis [J]. Materials & Design, 2018, 137: 286−297.

[40] LIU F C, CHENG H M, YU X B, YANG G, HUANG C P, LIN X, CHEN J. Control of microstructure and mechanical properties of laser solid formed Inconel 718 superalloy by electromagnetic stirring [J]. Optics and Laser Technology, 2018, 99: 342−350.

[41] GAUMANN M, HENRY S, CLETON F, WAGNIERE J D, KURZ W. Epitaxial laser metal forming: Analysis of microstructure formation [J]. Materials Science and Engineering A, 1999, 271: 232−241.

[42] ALI U, MAHMOODKHANI Y, SHAHABAD S I, ESMAEILIZADEH R, LIRAVI F, SHEYDAEIAN E, HUANG K Y, MARZBANRAD E, VLASEA M, TOYSERKANI E. On the measurement of relative powder-bed compaction density in powder-bed additive manufacturing processes [J]. Materials & Design, 2018, 155: 495−501.

[43] DINDA G P, DASGUPTA A K, MAZUMDER J. Laser aided direct metal deposition of Inconel 625 superalloy: Microstructural evolution and thermal stability [J]. Materials Science and Engineering A, 2009, 509: 98−104.

[44] SINDO Kou. Welding metallurgy [M]. 2nd ed. Hoboken, New Jersey: John Wiley & Sons, Inc., 2003.

[45] SHAO J Y, YU G, HE X L, LI S X, CHEN R, ZHAO Y. Grain size evolution under different cooling rate in laser additive manufacturing of superalloy [J]. Optics and Laser Technology, 2019, 119: 1−10.

[46] KNAPP G L, MUKHERJEE T, ZUBACK J S, WEI H L, PALMER T A, DE A, DEBROY T. Building blocks for a digital twin of additive manufacturing [J]. Acta Materialia, 2017, 135: 390−399.

[47] ACHARYA R, BANSAL R, GAMBONE J J, DAS S. A coupled thermal, fluid flow, and solidification model for the processing of single-crystal alloy CMSX-4 through scanning laser epitaxy for turbine engine hot-section component repair (Part I) [J]. Metallurgical and Materials Transactions B, 2014, 45: 2247−2261.

[48] SEGERSTARK A, ANDERSSON J, SVENSSON L E, OJO O. Microstructural characterization of laser metal powder deposited Alloy 718 [J]. Materials Characterization, 2018, 142: 550−559.

[49] ABOLFAZL S, MAHMOOD S, MAHDI S A. Effects of heat treatment on microstructure and mechanical properties of Inconel 625 alloy fabricated by wire arc additive manufacturing process [J]. Transactions of Nonferrous Metals Society of China, 2020, 30: 3016−3030.

[50] RAPPAZ M, DAVID S A, VITEK J M, BOATNER L A. Development of microstructures in FE-15NI-15CR single-crystal electron-beam welds [J]. Metallurgical Transactions A, 1989, 20: 1125−1138.

[51] WANG Guo-wei. Laser prototyping technology of nickel-base single crystal superalloys and simulation [D]. Beijing: University of Science and Technology of China, 2018. (in Chinese)

[52] KUMARA C, SEGERSTARK A, HANNING F, DIXIT N, JOSHI S, MOVERARE J, NYLEN P. Microstructure modelling of laser metal powder directed energy deposition of alloy 718 [J]. Additive Manufacturing, 2019, 25: 357−364.

激光功率对一种新型增材制造专用镍基高温合金显微组织和拉伸性能的影响

吴 彬[1,2]，梁静静[1,3]，周亦胄[1]，杨彦红[1,3]，李金国[1,3]，孙晓峰[1]

1. 中国科学院 金属研究所 师昌绪先进材料创新中心，沈阳 110016；
2. 中国科学技术大学 材料科学与工程学院，沈阳 110016；
3. 中国科学院 太空制造技术重点实验室，北京 100094

摘 要：研究在不同激光功率下某一新型增材制造专用高温合金的组织和拉伸性能。通过 X 射线衍射和电子扫描显微镜等手段，证实合金不含明显裂纹；合金组织由典型的定向生长非平衡凝固的枝/胞晶组织构成。枝晶间和枝晶干分别富集元素 Nb、Si、Ti 和 Al、Cr、Co。当激光功率较低时，合金的胞状晶排列整齐，一次枝晶间距(PDAS)小，孔隙率大，强度高、伸长率低；随着激光功率的增加，PDAS 增大，孔隙率降低，强度下降、伸长率提高；当激光功率更大时，Marangoni 对流效应增强并对组织和性能产生独特的影响，导致合金的胞状晶排列趋于紊乱，同时 PDAS 减小，孔隙率较大，强度值较高、伸长率较低。合金小的 PDAS 有利于减弱元素微观偏析、细化组织、提高合金强度。拟合了 PDAS 和屈服强度(YS)的关系公式，探讨了合金组织中同心花样环的形成机制。

关键词：Marangoni 对流；熔池；激光功率；一次枝晶间距(PDAS)；偏析

(Edited by Bing YANG)